Composites Science and Technology 248 (2024) 110466

Contents lists available at ScienceDirect

Composites Science and Technology

journal homepage: www.elsevier.com/locate/compscitech

Electrical and thermal behaviour of Z-pin reinforced carbon-fibre composite laminates under fault currents

Mudan Chen [a,*], Zhaobo Zhang [b,**], Bing Zhang [a,c], Giuliano Allegri [a], Xibo Yuan [b], Stephen R. Hallett [a]

[a] Bristol Composites Institute, University of Bristol, Bristol, BS8 1TR, UK
[b] Electrical Energy Management Group, University of Bristol, Bristol, BS8 1UB, UK
[c] School of Mechanical Engineering, University of Leeds, LS2 9JT, UK

ARTICLE INFO

Keywords:
A. Multifunctional composites
A. Laminate
B. Electrical properties
B. Thermal properties
Z-pin

ABSTRACT

Carbon-fibre reinforced polymer (CFRP) composites typically have poor electrical conductivity, primarily due to the conductive carbon fibres being separated by the insulating polymer matrix material. This is even more so in the case of interlayer toughened material systems that have an increased interlaminar spacing between the conductive carbon fibre layers. To mitigate the poor electrical conductivity of CFRP composites, the behaviour of Z-pinned laminates under electrical current was here studied experimentally. The in-plane and through-thickness fault currents were investigated for a quasi-isotropic (QI) composite laminate made from M21/IMA prepreg. Two kinds of pin materials (T300/BMI composite and copper) were used at two different volume fractions (0.1 % and 0.25 %). The pins reduced the through-thickness current resistance by two orders of magnitude, with a much smaller data variation, and up to one order for the in-plane direction. Through the use of electrically insulated pins, it was found that the electrical conductivity enhancement is caused by the fibre crimping around the pin and is unrelated to the pin material. Z-pins decreased the temperature increment caused by Joule heating during fault currents, thereby ensuring structural safety.

1. Introduction

The use of electrical power in aircraft is on the rise to boost overall efficiency, and cut fuel consumption, therefore reducing greenhouse gas emissions. It also provides better control performance and reduces maintenance. Thus, more electric aircraft (MEA) or all electric aircraft (AEA) are being developed worldwide, together with the adoption of electric propulsion systems [1]. In parallel, there has been a trend towards greater use of non-metallic composite materials, particularly carbon-fibre reinforced polymers (CFRP), to reduce structural weight. One of the advanced MEAs, Boeing 787, has more than 50 % of its structure built of CFRP. This results in a 20 % reduction in structural weight and an improvement of 10–12 % in total aircraft efficiency [2].

Continuous electrical current conduction through the CFRP may cause localised Joule heating that results in matrix degradation and can ultimately lead to structural failure. To ensure that electrical current does not pass through CFRP in the event of an electrical fault, bulky cable harnesses and heavy raceways are used extensively to form a current return network via existing metallic structures. Additional weight and volume are added to the system and advantages of mechanical performance attributable to the usage of CFRP are weakened [3,4]. Thus, the aerospace industry is promoting the creation of an embedded system by integrating electrical power systems with the aircraft's structural components [4]. It allows CFRP components to join the current return path under electrical fault conditions. The high impedance of CFRP will lead to a low electrical fault current that is difficult to detect with traditional grounding topology; meanwhile, the Joule heating effect still exits [4]. Therefore, it is crucial to enhance CFRP's electrical conductivity and have a thorough understanding of its behaviour under fault currents before and after the conductivity enhancement.

The electrical conductivity of carbon fibre (6×10^4 S/m) is approximately three orders of magnitude lower than that of metals. The epoxy resin matrix, commonly employed in aerospace applications, is an

* Corresponding author.
** Corresponding author.
E-mail addresses: mudan.chen@bristol.ac.uk (M. Chen), zhaobo.zhang@bristol.ac.uk (Z. Zhang).

https://doi.org/10.1016/j.compscitech.2024.110466
Received 8 October 2023; Received in revised form 23 January 2024; Accepted 24 January 2024
Available online 26 January 2024

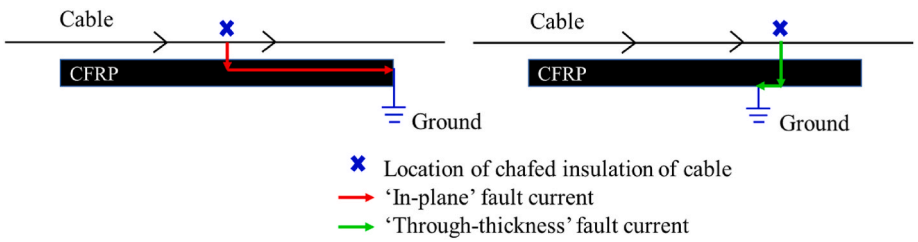

Fig. 1. Path of the fault current through a CFRP structure.

insulator (electrical conductivity of 4.9×10^{-16} S/m) [5]. The fibres and different plies are separated by the resin matrix, resulting in pronounced electrical anisotropy for CFRP structures. For instance, the longitudinal, transverse, and through-thickness electrical conductivities of a unidirectional (UD) laminate made of IM7/8552 prepreg are reported to be 3×10^4 S/m, 3.5 S/m, and 0.8 S/m, respectively [6]. In contrast, metals have an isotropic conductivity at the order of 10^7 S/m (e.g., 6×10^7 S/m for the copper) [5]. Thus, the electrical behaviour of CFRP is more complex compared to that of metals. Piche et al. [7] predicted the dynamic electrical resistance of a CFRP under a short circuit by combining a 3D linear-wired numerical approach with an analytical model. Fibres, connections between fibres in a ply, and connections between plies were represented with thin wire networks, allowing the model to take into account the different orientations of each ply. However, a homogeneous electrical conductance across the thickness over the entire surface was assumed in the 3D model. Consequently, the model may not accurately represent scenarios where contacts are not uniformly distributed between plies. Jones et al. [6] experimentally investigated the fault current response of unidirectional CFRP. A range of voltages was applied across the CFRP with various initial power levels. The result shows that the electrical current flows predominantly through the top layer of CFRP. The electrical resistance of CFRP changes with time due to Joule heating. The time to reach the glass transition temperature (T_g) against the initially applied voltages/power was found to follow a nonlinear decaying power relationship.

A variety of methods have been studied to enhance the electrical conductivity of laminates [5], such as adding conductive fillers to the polymer matrix, using conductive resins and conductive interleaves. As a very effective through-thickness reinforcement technology, Z-pinning has been studied broadly to extend its multifunctional applications [8], such as electrical [9,10], thermal [11–13] and magnetic properties [14], as well as delamination detection [15–19] and self-healing [20–22]. Pegorin et al. [9] carried out experimental studies on the use of Z-pins to enhance the electrical properties of carbon-epoxy laminate. The through-thickness conductivity increased linearly with the volume content and the conductivity of Z-pins, while the in-plane conductivity was not enhanced by the pins due to the interfacial cracks around the pins, which were generated due to the mismatch of thermal expansion coefficient between the pins and laminate.

However, there is a lack of research on the fault current response of through-thickness reinforced composites. This study investigated electrical and consequential thermal behaviour of Z-pinned laminates under fault currents for the first time. Specimens with two pin materials at two areal densities were measured under a variety of in-plane and through-thickness fault currents, in comparison with unpinned ones. Specifically, specimen preparation is introduced in Section 2. Resistance measurement results are presented in Section 3, then fault current tests and results are illustrated in Section 4.

2. Specimen preparation

The specimens used in this study were made of unidirectional M21/IMA prepreg (HexPly® M21/34 %/UD194/IMA-12K) [23] with a quasi-isotropic (QI) stacking sequence of $[+45°/90°/-45°/0°]_{3s}$. The M21/IMA material has a layer of thermoplastic toughening particles at the resin rich boundary between plies [24]. This interleaving method is a well-known way to increase the interlaminar toughness of cured laminates [25], but the thick interleaf layer has a negative influence on electrical conductivity.

Two types of pins with the same diameter of 0.28 mm, i.e., copper (from WIRES) and the more conventional T300/BMI were employed to make Z-pinned specimens. The pin-to-pin distances were designed to be 8 mm and 5 mm respectively, which gives the pinning areal densities of 0.1 % and 0.25 %. Thus, five categories of samples were manufactured: unpinned (UP), copper low-density (COP-L) and high-density (COP-H) Z-pinned, carbon low-density (CAR-L) and high-density (CAR-H) Z-pinned. Due to the numerous variables involved in designing the fault current experiment, a square shape has been consistently adopted in the literature [6,7]. Manufacturing large Z-pinned specimens demands a significantly larger effort than for unpinned coupons. Adopting a size of 30 × 30 mm provides sufficient space for electrode arrangement. These dimensions, together with the two designed pin-to-pin distances, enable exploration of two distinct relative arrangements of pins and electrodes, i.e., aligned or not aligned in the fibre direction of the top ply. Thus, considering the above test design and specimen manufacturing requirements, the Z-pinned specimens in this research are designed with a length and width of 30 mm × 30 mm and an intermediate thickness of 4.5 mm.

The specimen manufacturing was as follows: (1) Layup the prepreg in sequence on an aluminium plate and de-bulk for 15 min in a vacuum bag after every four plies. (2) Using a hot plate beneath, gently soften the laminate, and manually insert the pin through the entire thickness of the laminate into a pre-drilled hole made by an Instron-powered drilling rig. (3) Cure the laminate in an autoclave under a modified Hexcel cure cycle [23] by adding 30 min to the dwelling stage to compensate for the influence of silicon rubber sheets placed on the top and bottom of the laminate for the protection of pin ends. (4) Trim the protruding pin ends with wire scissors and cut individual samples from the cured laminate with a diamond saw. After cure, each ply has a nominal thickness of 0.188 mm.

3. Resistance measurement

3.1. Measurement set-up

Similar to the scenario that Jones et al. considered in Ref. [6], the rail-to-ground fault inside a CFRP structure was investigated, which can be caused by the vibration and chafing of an insulator. Here the current path is extended to in-plane and through-thickness directions, respectively, as shown in Fig. 1.

The study in Ref. [6] was based on a unidirectional laminate. Here, a QI stacking sequence, which is more representative of that used in the composites industry, was investigated, as well as the effects of Z-pins on the fault current performance of composites. The scenario is more complex for a QI stacking sequence with +45° surface plies. Thus, nine current input areas were designed on the top surface to take into consideration different circumstances caused by chafing of an electric cable, for example. The exit points were on the side and bottom surfaces,

Fig. 2. Sample photos: (a) COP-L top surface, (b) COP-H top surface, (c) COP-H bottom surface.

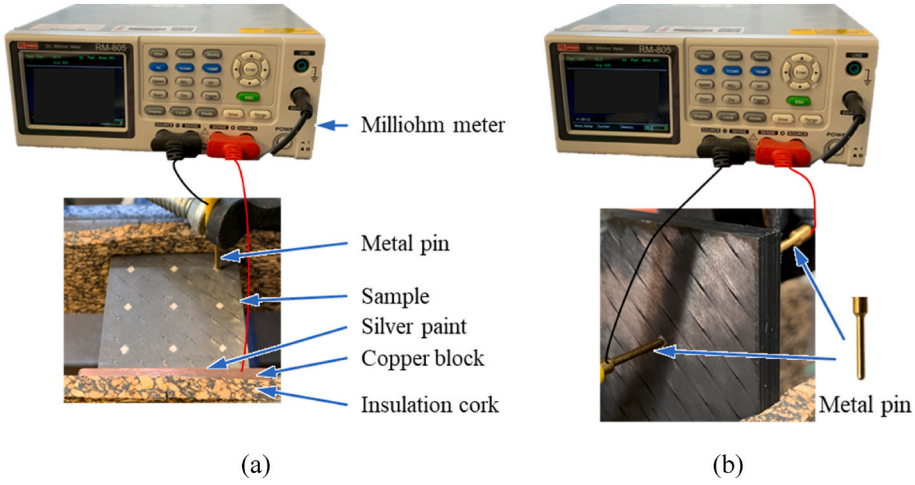

Fig. 3. Resistance measurement set-up: (a) in-plane, (b) through-thickness.

Table 1
Experimental results of the through-thickness resistance.

	Pos.	1	2	3	4	5	6	7	8	9
UP	*R* (Ω)	1760	1767	1798	1772	1758	1767	1810	1771	1759
	C.V. %	39.0	39.1	38.5	39.3	38.9	39.1	38.7	39.3	39.0
COP-L	*R* (Ω)	32.3	41.6	57.6	37.0	31.4	43.0	54.3	38.0	32.7
	C.V. %	12.1	10.6	20.1	5.2	12.1	12.4	15.4	4.5	11.3
COP-H	*R* (Ω)	21.6	21.7	30.0	26.0	20.7	23.8	31.8	23.4	21.8
	C.V. %	14.8	11.6	20.8	19.7	16.8	21.8	9.2	10.9	21.7
CAR-L	*R* (Ω)	23.1	26.4	36.0	26.7	22.4	26.2	40.0	26.3	23.4
	C.V. %	20.7	17.5	23.1	15.1	21.4	17.2	22.3	15.8	18.2
CAR-H	*R* (Ω)	15.6	16.6	20.5	16.5	15.6	16.7	19.3	16.2	16.0
	C.V. %	9.8	13.2	9.1	6.8	8.2	12.6	8.1	6.7	8.2

Table 2
Experimental results of the in-plane resistance.

	Pos.	1	2	3	4	5	6	7	8	9
UP	*R* (Ω)	8.9	3.1	3.2	33.8	7.7	1.9	76.2	33.8	8.4
	C.V. %	56.6	33.3	21.1	40.0	56.4	17.1	50.4	39.9	47.2
COP-L	*R* (Ω)	6.0	4.7	3.1	11.3	4.6	3.8	28.1	12.9	5.7
	C.V. %	40.7	30.8	19.3	43.9	2.3	28.4	30.2	24.3	23.9
COP-H	*R* (Ω)	4.3	2.9	3.2	7.5	3.5	2.5	14.0	7.2	3.2
	C.V. %	20.5	16.5	19.9	33.0	27.0	26.0	32.0	33.1	27.9
CAR-L	*R* (Ω)	4.3	4.2	3.1	8.4	3.6	3.8	22.3	8.5	3.4
	C.V. %	4.5	11.5	65.6	4.7	5.7	6.3	19.1	9.2	9.6
CAR-H	*R* (Ω)	3.3	2.5	2.3	4.4	2.8	2.0	7.3	4.2	2.9
	C.V. %	22.5	17.4	23.2	1.6	20.6	16.1	6.0	7.4	1.4

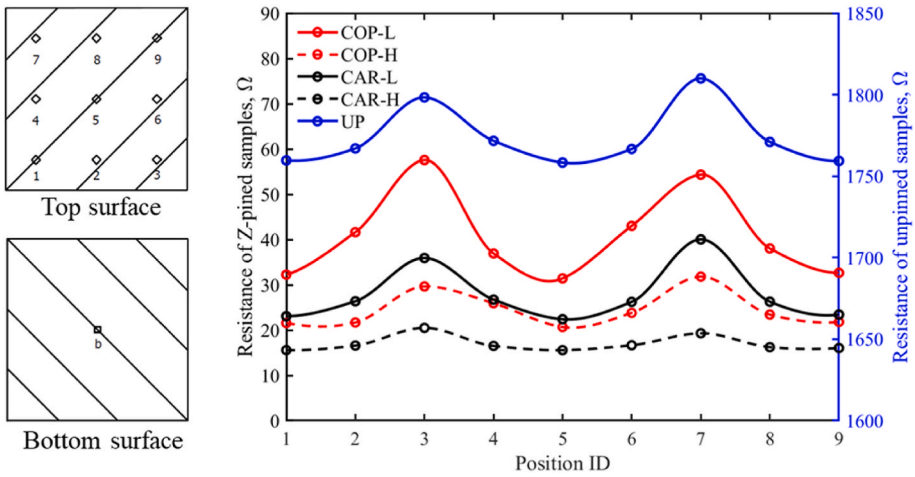

Fig. 4. Experimental plot of the through-thickness resistance.

which represented the in-plane and through-thickness fault currents, respectively.

Epoxy on the top and bottom plies was carefully removed by a polisher to mimic the cable chafing effect. A thin layer of silver was painted uniformly on each 1 × 1 mm square box. In order to achieve a good painting quality, the to-be-painted area was cut out from adhesive paper by a laser cutter, then the paper was pasted on the sample, afterwards the silver paste was brushed in the blank area. The top and bottom surfaces of Z-pinned samples with numbered silver paint electrodes are shown in Fig. 2.

For the electrical resistance measurement, a vice was used to clamp the sample in place, and metal pins were fixed to the electrodes using a magnetic stand to ensure secure contact, as illustrated in Fig. 3. The metal pin has a cylindrical shape with the diameter of 1 mm. It has a rounded tip, providing a point of contact with the silver paste while minimising any potential damage to the paste. When measuring the in-plane resistance (Fig. 3 (a)), each of the top surface electrodes was connected to a probe of a milliohm meter in turn. The side surface of the specimen was coated with silver paste and a copper block was tightly clamped to it. This was done to reduce the contact resistance and ensure consistency in the measurements. For the through-thickness measurement (Fig. 3 (b)), a probe was connected to each of the top surface electrodes in turn and the output was recorded from a probe on the central bottom electrode using metal pins. Each measurement was taken twice to ensure accuracy, and a negligible bias was achieved. Three samples were tested for each group, the measured through-thickness and in-plane average resistances and variations are given in Table 1 and Table 2, respectively.

3.2. Resistance results of the through-thickness direction

Table 1 shows that the through-thickness resistances of the unpinned samples are in the order of 10^3 Ω. After adding pins, the resistance decreased significantly at all nine locations (less than 10^2 Ω). The resistance variation of unpinned samples is much higher than Z-pinned ones, comparing the coefficients of variation (C.V.) in Table 1. The reason will be discussed later.

The mean value of measured resistance is plotted in Fig. 4. Note that the curves connecting the individual measurement data have no physical meaning, and they are only used for comparing data and illustrating the trend more intuitively. Due to the large difference between unpinned and Z-pinned samples, the unpinned data is plotted using a secondary y-axis on the right. The plot has a symmetric trend which is consistent with distribution of top-surface electrodes, i.e., positions 1 & 9, 2 & 8, 3 & 7, and 4 & 6 are symmetrical about position 5 (or position b). The resistance of positions 3 & 7 is the highest, because the current needs to travel furthest in the direction perpendicular to surface-ply fibres to reach the bottom surface exit electrode b. It also implies that the current path of the top ply dominates the global result.

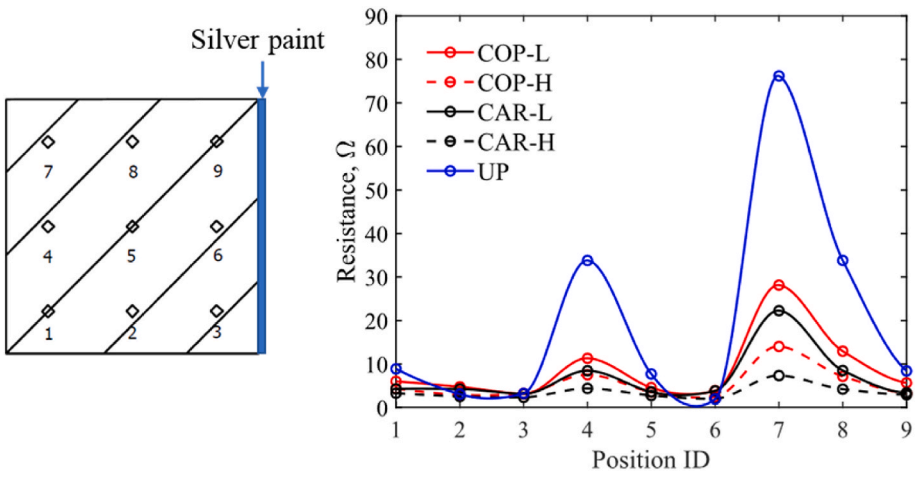

Fig. 5. Experimental plot of the in-plane resistance.

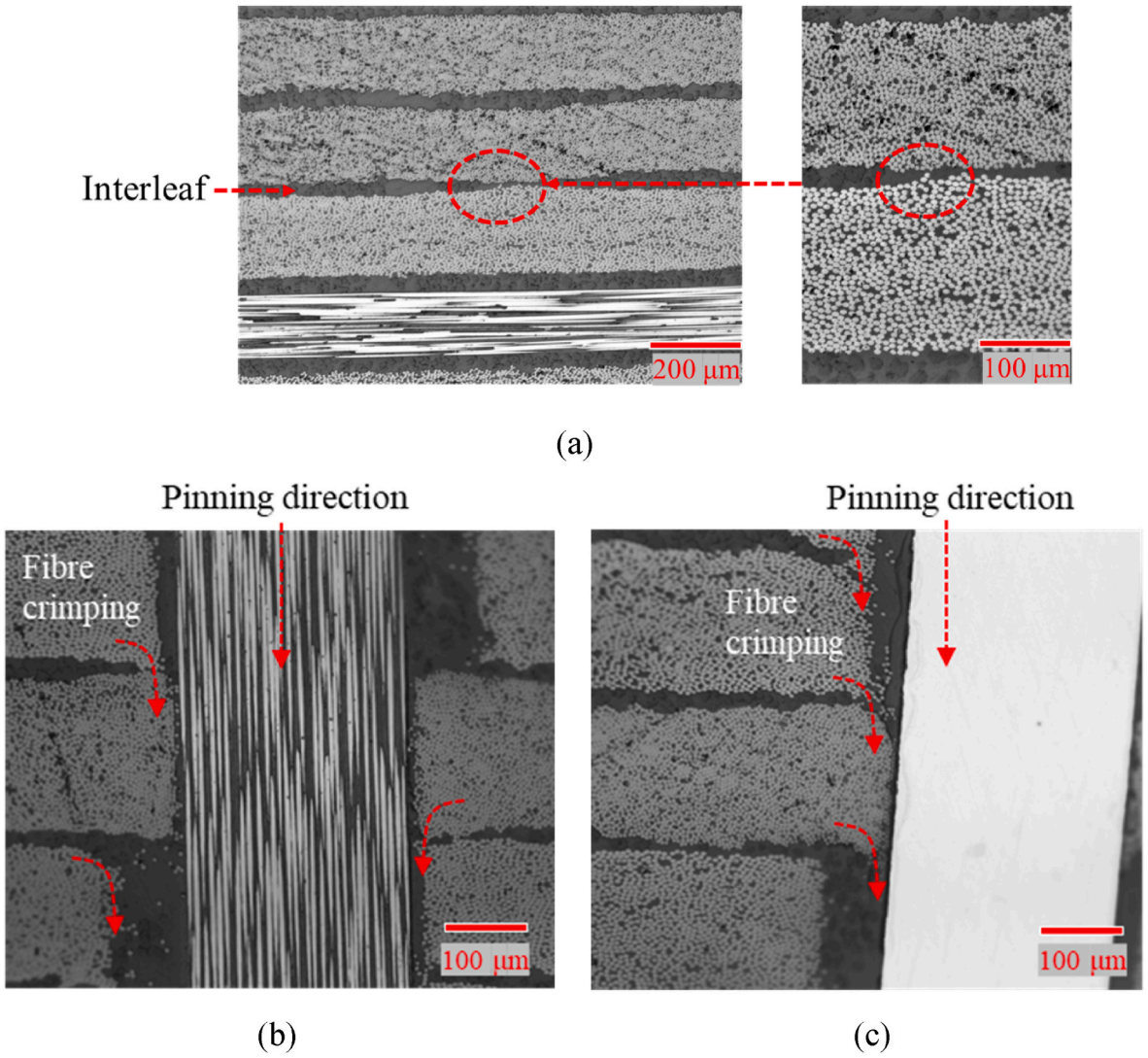

Fig. 6. Microscope images of sample cross-sections: (a) unpinned, (b) carbon-fibre Z-pinned, (c) copper Z-pinned.

3.3. Resistance results of the in-plane direction

For the in-plane direction (Table 2), the Z-pins also reduce the resistance, although the amount is not as much as the through-thickness direction. The similar top layer dominated behaviour was observed in Fig. 5. If the current can pass from fibres at the chafing area to the exit electrode directly, the resistance is low, such as positions 1, 2, 3, 5, 6 and 9. The resistances associated with positions 4, 7 and 8 of Z-pinned samples are much smaller than unpinned ones, because the current is able to transfer through the thickness, then go through the fibres of other layers to the side exit electrode.

3.4. Result discussion

3.4.1. Influence of Z-pin material and areal density

The resistance of copper Z-pinned samples is higher than carbon-fibre Z-pinned samples in both in-plane and through-thickness directions (comparing the red and black curves in Figs. 4 and 5), while the electric conductivity of a copper pin is much higher than that of a carbon-fibre pin [9]. The copper pins therefore didn't function as expected for the through-thickness current transfer.

As reported in the literature [8], the laminate fibres are forced to bend around the pin during insertion. The resin pocket around the pin and the interfacial cracking impedes the current flow within the ply. In order to see the detailed information around the pin, the samples were cut into slices and potted with epoxy resin, then polished to make the individual fibres visible. The microscope images of the cross sections are given in Fig. 6.

It shows that there is randomly localised interlaminar fibres touching inside the unpinned sample (Fig. 6 (a)). Since they are randomly distributed, the through-thickness resistance of unpinned samples varies a lot (as shown in Table 1). In Fig. 6 (b, c), due to the fibres bending around the pin (known as crimping), more fibre touching was observed in the through-thickness direction for both carbon-fibre Z-pinned and copper Z-pinned samples. Thus, the electrical conductivity is mainly related with the pinning quality, e.g., the misalignment angle. As the copper pin is soft, although great care was taken during insertion, it was slightly bent, and the misalignment angle is higher than that of carbon-fibre pins, as shown in the microscope images of Fig. S2 in the supplementary document.

For a quantitative comparison, the resistance of a reference laminate, pinned with enamelled copper wires, was measured. This wire has the same size as bare copper wire at 0.28 mm diameter, with a polymer layer coated on the outside, making the pin electrically isolated on its surface. The measured resistance of the enamelled copper pinned specimens was very close to that of the uncoated copper pinned ones (the result is given in the supplementary document). It again demonstrates that the pin itself is not directly engaged in the current path. The fibre-to-fibre

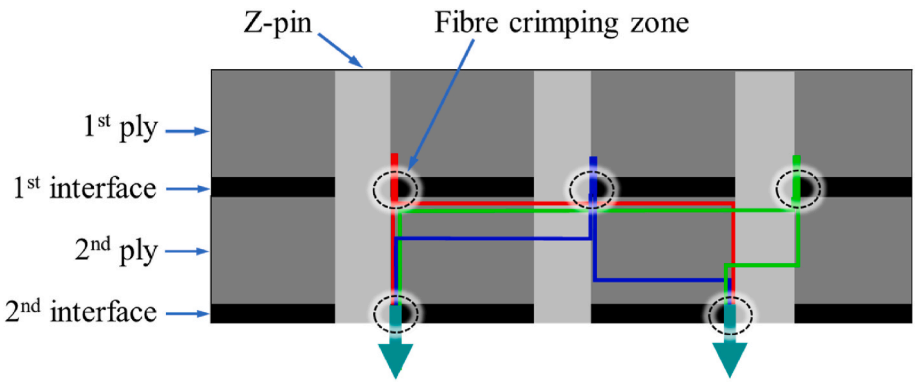

Fig. 7. Schematic diagram of the current path inside the first two plies of a Z-pinned specimen.

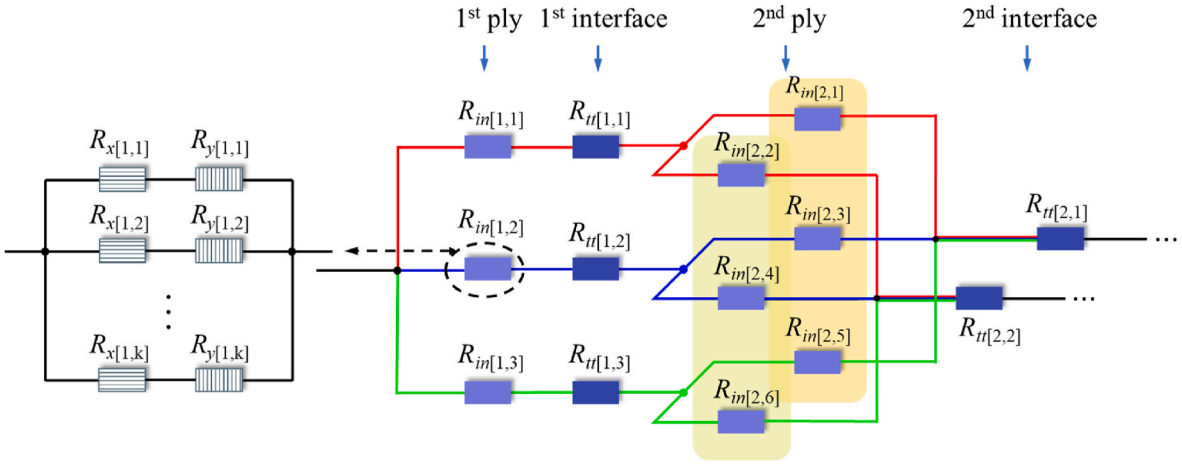

Fig. 8. 3D topology electrical resistance model.

connections, instead of the pins, are the main current flow path for through-thickness conduction. The lower through-thickness resistance of enamelled copper pin compared to the bare copper pin is because the coating outside makes the enamelled copper pin stiffer than the bare copper pin, resulting in less bending of the pin and reduced misalignment. A lesser degree of misalignment will shorten the distance for current flow in the through-thickness direction, consequently decreasing resistance.

In addition, the high-density Z-pinned samples have lower resistance than low-density ones for both pin materials (comparing the solid and dashed curves with the same colour in Figs. 4 and 5), because the higher areal density creates more fibre connections in the vicinity of the pins.

3.4.2. Current path analysis

For an intuitive view, an illustration of the current transfer path of the first two plies and interfaces is given in Fig. 7, assuming that there are three and two fibre touching zones at the 1st and 2nd interfaces, respectively. The red, blue and green lines represent the current paths from the injection position. Specifically, the current will pass through the top ply (1st ply), then the pin vicinity with fibre touching at the 1st interface, and afterwards within the 2nd ply to find the conductive path in the 2nd interface.

The 3D topology electrical resistance model is drawn in Fig. 8, in which $R_{in[i,m]}$ and $R_{tt[j,n]}$ are the m^{th} equivalent resistor of i^{th} ply and n^{th} the resistor of the j^{th} interface, respectively. From the diagram, it can be seen that if the number of fibres touching zones within two adjacent interfaces are a and b, there is a * b current paths generated inside the ply in-between. For instance, there are 6 current paths in the 2nd ply as shown in Fig. 8. When inserting pins, the interlaminar resistance R_{tt} is reduced significantly, thus the total through-thickness resistance is much smaller. If adding more pins (increasing the pinning areal density), there are more current paths generated.

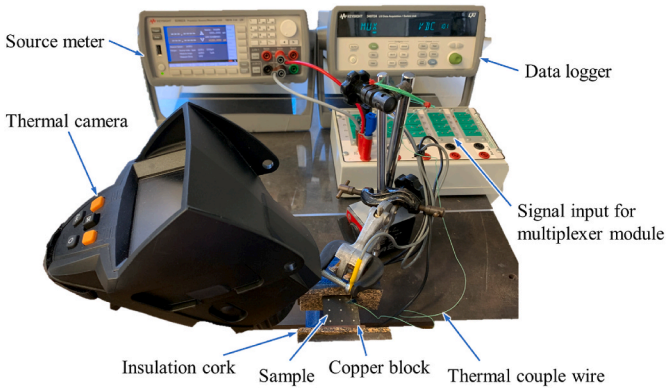

Fig. 9. Fault current response test set-up.

4. Fault current response test

4.1. Test set-up

The resistance measurement results above indicate that the resistance reduction of position 7 by Z-pins is the greatest for both in-plane and through-thickness directions, as shown in Figs. 4 and 5. Thus, a constant current was injected from this position to simulate the in-plane

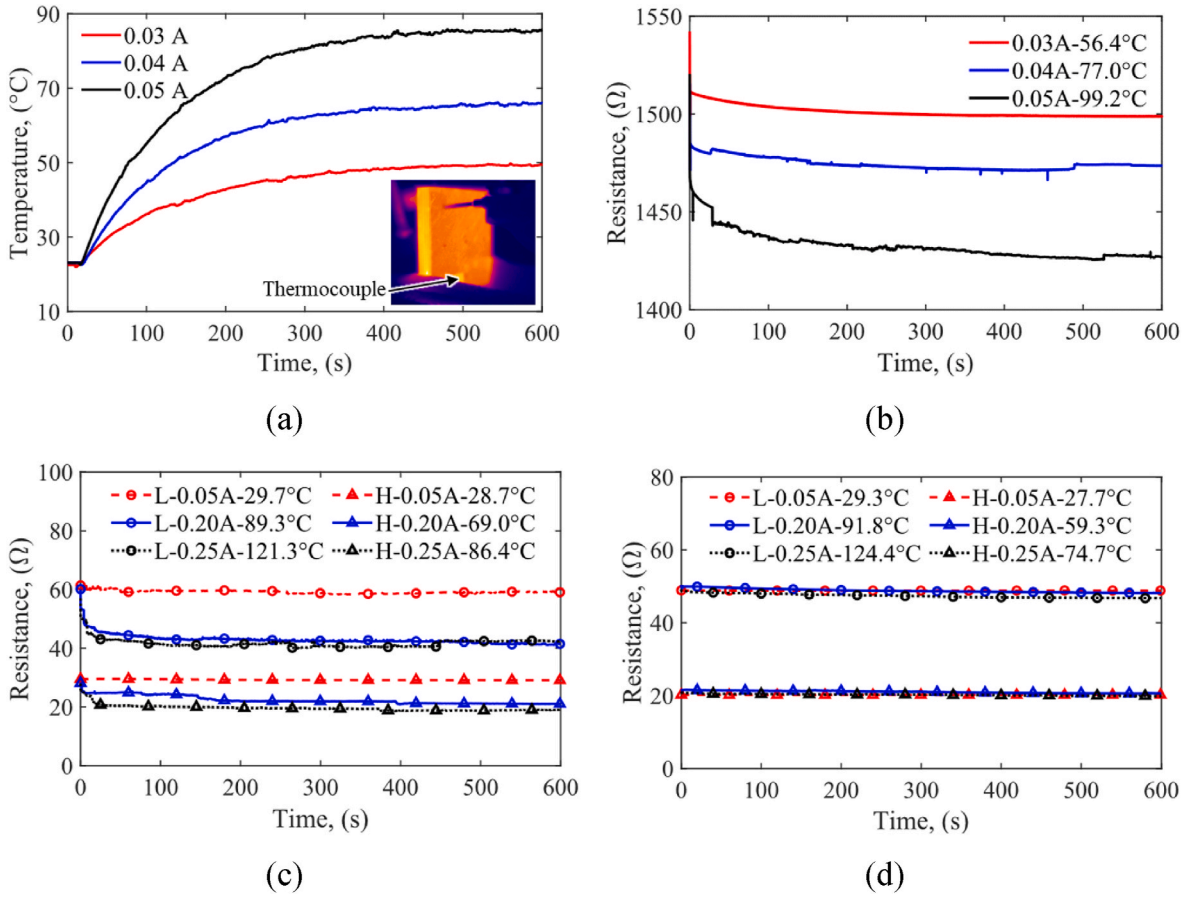

Fig. 10. (a) Temperature versus time plot of an unpinned specimen, through-thickness fault current response test results of (b) unpinned, (c) copper and (d) carbon-fibre Z-pinned specimens, (L: low density, H: high density).

Table 3
Current injection data in the through-thickness direction.

	R_O (Ω)	I_f (A)	P_O (W)	T_u (°C)
UP	1577	0.03	1.42	56.4
	1577	0.04	2.52	77.0
	1577	0.05	3.94	99.2
COP-L	62.4	0.05	0.16	29.7
	62.4	0.2	2.50	89.3
	62.4	0.25	3.90	121.3
COP-H	30.1	0.05	0.08	28.7
	30.1	0.2	1.20	69.0
	30.1	0.25	1.88	86.4
CAR-L	49.8	0.05	0.12	29.3
	49.8	0.2	1.99	91.8
	49.8	0.25	3.11	124.4
CAR-H	21.2	0.05	0.05	27.7
	21.2	0.2	0.85	59.3
	21.2	0.25	1.33	74.7

and through-thickness fault current response of unpinned and Z-pinned laminates. The test set-up is shown in Fig. 9. The current was supplied with a source meter (KEYSIGHT B2902A). A data logger was used to collect the data of voltage and temperature (when a thermocouple was applied), and a thermal camera was employed to capture the temperature distribution on the samples' surface.

The current injection lasted for 10 min (600 s) for each test. Fig. 10 (a) shows the temperature-versus-time plot of a hot spot on the surface of an unpinned sample at different levels of current. A thermocouple was placed upon this spot, using high-temperature tape for the measurement. The plot shows that the temperature grows very rapidly at the beginning, then becomes stable after 400 s. A period of 10 min is long enough to achieve a stable temperature state.

The instantaneous power $P(t)$ has the following relationship with the fault current I_f and resistance $R(t)$:

$$P(t) = I_f^2 \bullet R(t) \tag{1}$$

In this case, $R(t)$ is a time dependent variable, and I_f is constant, controlled by the source meter accurately.

4.2. Test results of the through-thickness direction

4.2.1. Resistance versus time

As the through-thickness resistance of the unpinned samples is much higher than Z-pinned ones, in order to achieve a comparable level of power, the injected current for unpinned samples is smaller than Z-pinned ones. The injected current I_f, initial resistance R_o, initial power P_o, and the ultimate temperature T_u are summarized in Table 3. It shows that T_u increases with the current amplitude for each type of sample. When all types of samples were injected with the same current of 0.05 A, T_u of the unpinned sample goes up to 99.2 °C, which is much higher than that of Z-pinned samples (less than 30 °C). The pins effectively suppress the Joule heating effect and keep the resin in a safe temperature margin when there is a top-to-bottom fault current.

The resistance versus time is plotted in Fig. 10(b-d) with the injected current and ultimate temperature listed in the legend. In Fig. 10 (b), the resistance of unpinned samples decreases suddenly at the beginning, then tends to stabilise. The decrease is mainly caused by the thermal expansion, which enhances transverse and interlaminar fibre touching [26]. When the copper Z-pinned samples are under higher currents of 0.2 A and 0.25 A (Fig. 10 (c)), the resistance decreases at the beginning.

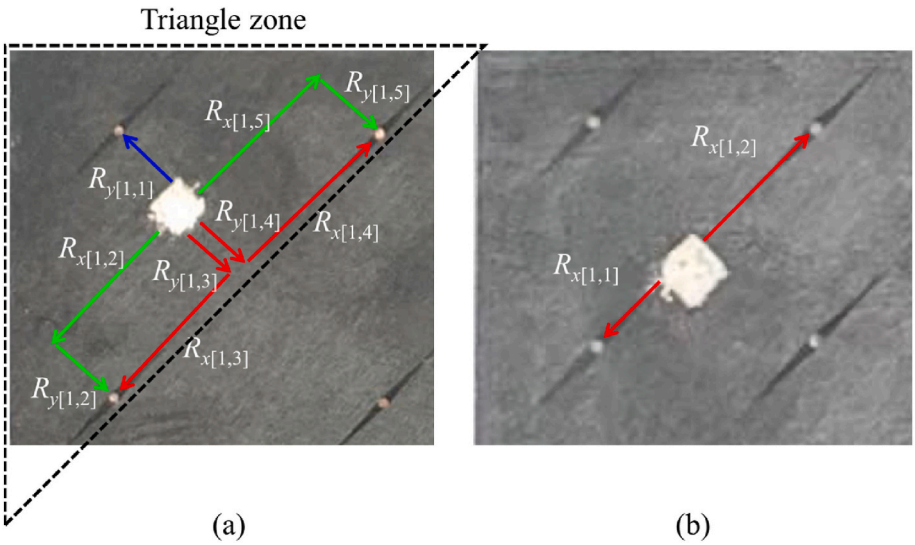

Fig. 11. Current flow diagram in the top surface of Z-pinned samples: (a) COP-L, (b) COP-H.

While the resistance of carbon-fibre Z-pinned sample remains relatively constant throughout the test (Fig. 10 (d)). The resistance drop of copper Z-pinned samples is mainly caused by the mismatch of the thermal expansion coefficient (CET) between the copper pin ($1.67e^{-5}\,^{\circ}C^{-1}$) [27] and the laminate ($0\,^{\circ}C^{-1}$ in the fibre direction, $3e^{-5}\,^{\circ}C^{-1}$ in transvers and through-thickness directions) [28]. Residual stress was generated at the pin/laminate interface during heating, enhancing the fibre touching of pin vicinity [8]. While the CETs of carbon-fibre pin and laminate are comparable, and the thermal expansion influence on the interface is negligible.

4.2.2. Heat flow analysis

Before examining the thermal images, the current flow within the top surface of Z-pinned samples is discussed first. As mentioned in Section 3, for Z-pinned samples, the current flows through the pinning vicinity via fibre touching. In Fig. 11 (a) showing a low-density Z-pinned sample, there is no direct path from the current injection point to the pins along the fibre direction, thus the current will flow both along fibres (x axis) and perpendicular to fibres (y axis), and the whole triangle zone is involved in the current transfer. While for high-density Z-pinned samples, the current can flow to two adjacent pins along the fibre direction only (Fig. 11 (b)).

The left picture of Fig. 8 gives an example of the electrical resistor model of the in-plane resistor $R_{in[1,2]}$. In general, the m^{th} equivalent in-plane resistor of i^{th} ply, $R_{in[i,m]}$, can be denoted with the resistors along and perpendicular to the fibre directions (R_x and R_y) as below, in which k is the number of conductive paths.

$$R_{in[i,m]} = \frac{1}{\frac{1}{R_{x[i,1]}+R_{y[i,1]}} + \frac{1}{R_{x[i,2]}+R_{y[i,2]}} \cdots + \frac{1}{R_{x[i,k]}+R_{y[i,k]}}} \tag{2}$$

Since the heat flow distribution of carbon-fibre and copper Z-pinned specimens are similar, the result of copper Z-pinned specimens is given in the supplementary document. Fig. 12 shows the thermal images of unpinned and carbon-fibre Z-pinned samples. The current injection (top) and exit (bottom) surfaces are on the left and right sides, respectively. The bright areas correspond to regions with the highest temperature change along the current conducting path. As discussed above, for the low-density Z-pinned sample, the top left triangle area including three pins is involved in the current transfer, which can be observed in Fig. 12 (c). While for the high-density Z-pinned sample, two pinned areas appear brighter in Fig. 12 (e). When looking at the bottom surfaces of pinned specimens (Fig. 12 (d, f)), the pinned areas exhibit higher temperature than their surroundings, because these fibre touching zones are engaged in transferring the current. Regarding the unpinned sample in Fig. 12 (a), the heat distribution is uniform for both surfaces. A single hot spot is visible on the side surface, located in one of the areas where fibres are randomly touching each other. It is notable that the heated area on the bottom surface is greatest for the high-density carbon-fibre case out of all the pinned samples, indicating that in this case the Z-pins have most significantly facilitated current flow through the thickness of the sample.

4.3. Test results of the in-plane direction

The current injection data from the in-plane direction tests is summarized in Table 4. Just like the through-thickness direction, the ultimate temperature T_u increases with the current amplitude. When the current is 0.2 A for all types of samples, T_u of the unpinned samples (99.1 °C) is much higher than the Z-pinned ones (maximum 56.8 °C).

The resistance versus time is plotted in Fig. 13. It also shows that the resistance of unpinned samples drops suddenly at the beginning, then becomes stable. In terms of the copper pinned samples, it has been illustrated in Fig. 10 (c) that the resistance decreases when temperature goes up for the through-thickness fault current. While the resistance doesn't change when it experiences an in-plane current, as shown in Fig. 13 (b). This implies that the current only goes through a few plies instead of the whole thickness under this circumstance, by comparing Fig. 10 (c) with Fig. 13 (b). On the other hand, the resistance of carbon-fibre pinned samples is still quite stable.

The thermal images of the top surface are presented in Fig. 14. In Fig. 14 (a), it has a random hot spot on the top surface of the unpinned samples, which is one of the through-thickness fibre touching areas. In terms of the carbon-fibre Z-pinned samples, the in-plane thermal images are quite similar to the through-thickness ones, since the current will transfer through the top surfaces firstly for both scenarios. The analysis of through-thickness fault current above is also applicable to the in-plane direction.

5. Conclusions

The behaviour of copper and carbon-fibre Z-pinned CFRP laminates under the in-plane and through-thickness fault currents has been investigated experimentally. Several conclusions could be drawn here: (1) The through-thickness resistance was reduced by two orders with Z-pins, due to the fibre crimping in the pin vicinity. The pin itself is not engaged in the current path network, because of the resin pocket and

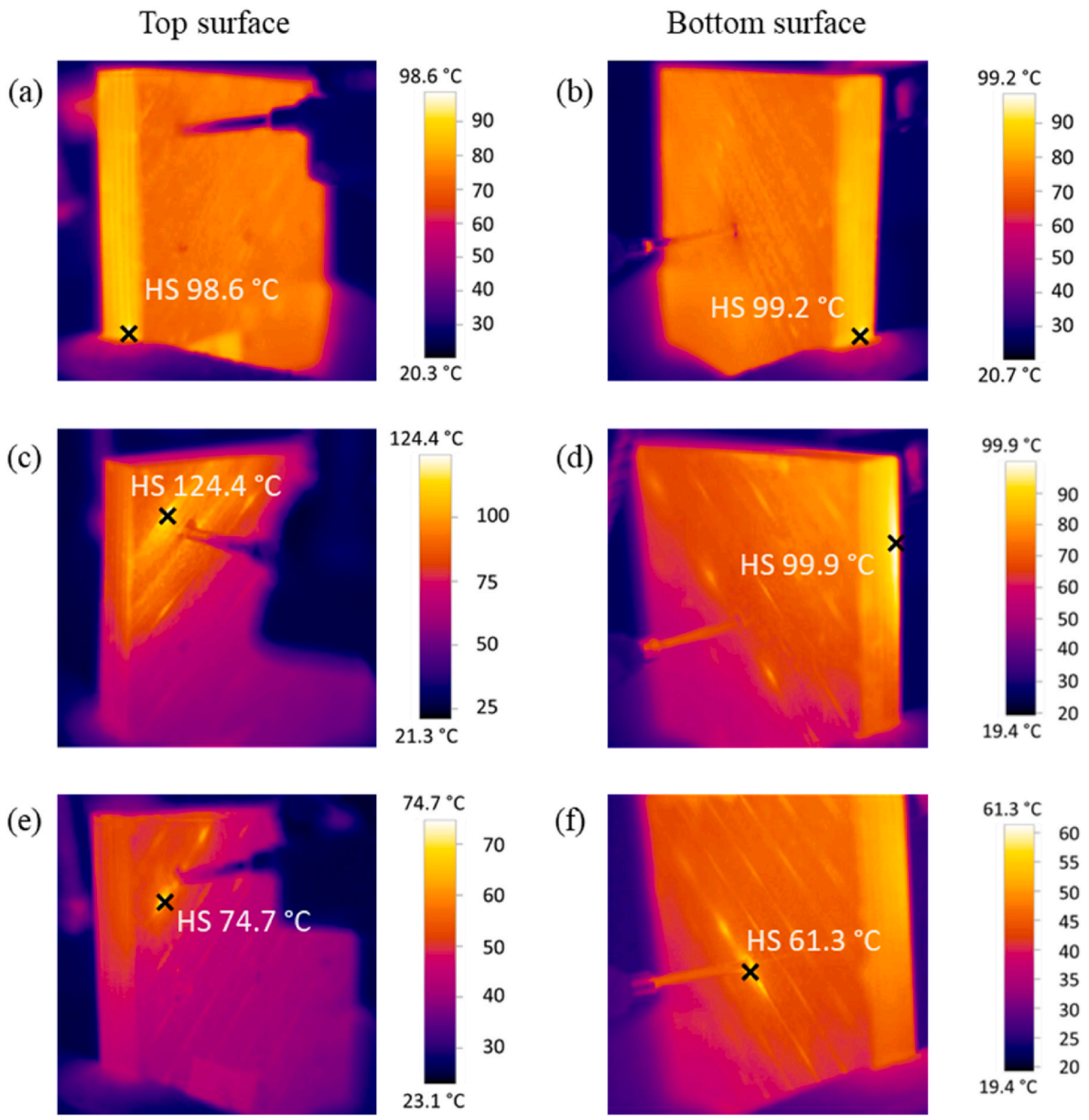

Fig. 12. Through-thickness thermal images: (a, b) UP-0.05 A, (c, d) CAR-L-0.25 A, (e, f) CAR-H-0.25 A.

Table 4
Current injection data in the in-plane direction.

	R_O (Ω)	I_f (A)	P_O (W)	T_u (°C)
UP	55.9	0.1	0.56	43.0
	55.9	0.2	2.24	99.1
COP-L	27.2	0.2	1.09	56.8
	27.2	0.3	2.45	99.1
	27.2	0.4	4.35	149.4
COP-H	14.0	0.2	0.56	44.9
	14.0	0.3	1.26	70.0
	14.0	0.4	2.24	106.6
CAR-L	21.8	0.2	0.87	53.8
	21.8	0.3	1.96	91.4
	21.8	0.4	3.49	132.6
CAR-H	8.2	0.2	0.33	41.0
	8.2	0.3	0.74	62.3
	8.2	0.4	1.31	95.0

interfacial cracking. (2) The in-plane conductivity was improved, not as significantly as the through-thickness direction, but still obviously for some chafing locations, for instance, up to one order at position 7. (3) The resistance decreases with the pining areal density, as more conductive paths were generated. (4) When suffering from the same amount of fault current, the temperature of unpinned sample is much higher than Z-pinned ones. (5) The heat flow distribution on the outer surfaces of Z-pinned laminates differs from the unpinned ones. The relative positioning of the pins and chafing areas is the determining factor.

In summary, this work shows that there is a notable enhancement of the electrical conductivity of CFRP laminates with Z-pins inserted, especially in the through-thickness direction. The conductivity improvement reduces the temperature increase due to Joule heating under fault currents. Unlike other conductivity enhancements, such as metal meshes that have only one function and increase the laminate weight, the Z-pins also have a beneficial influence on the laminate's through-thickness mechanical properties. In the future, a quantitative study could be conducted to investigate the effects of pin misalignment

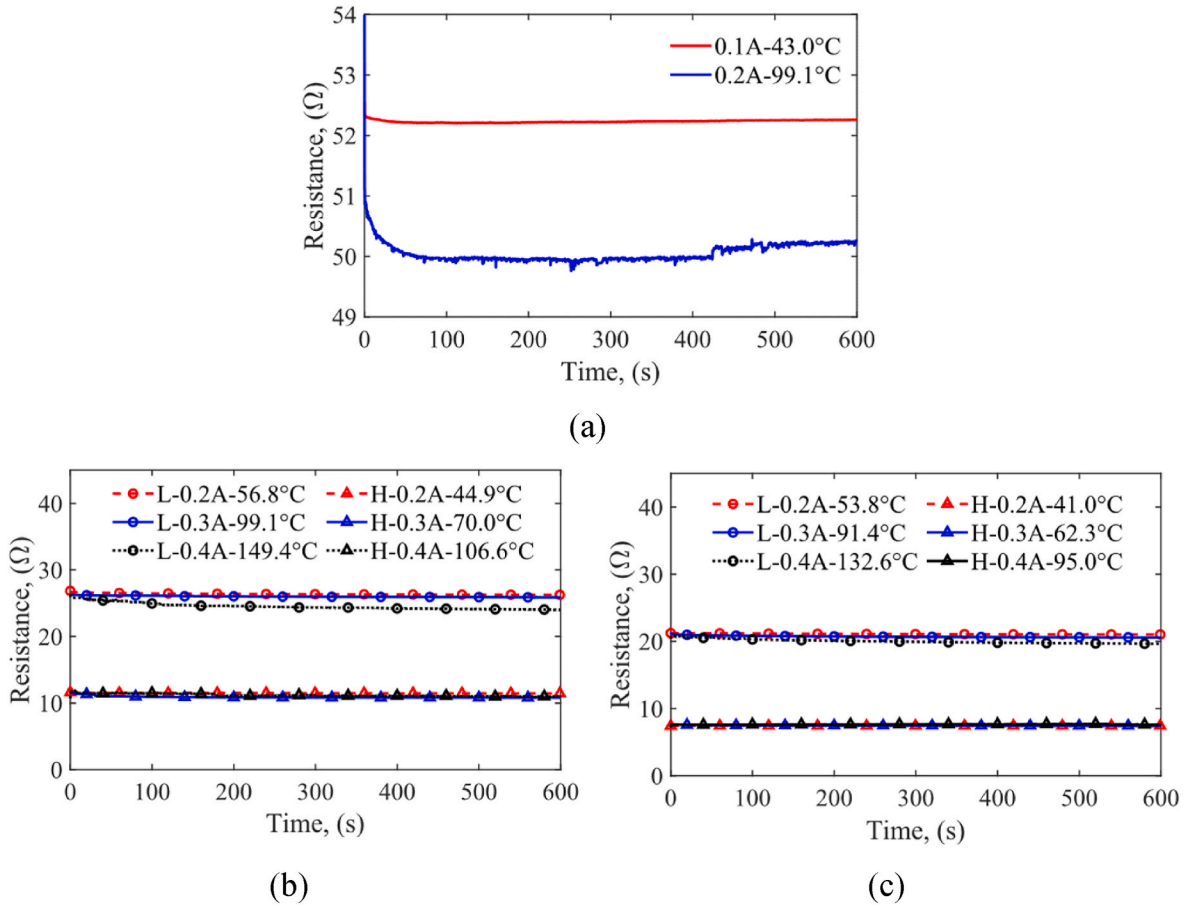

Fig. 13. In-plane fault current response test results of (a) unpinned, (b) copper and (c) carbon-fibre Z-pinned specimens, (L: low density, H: high density).

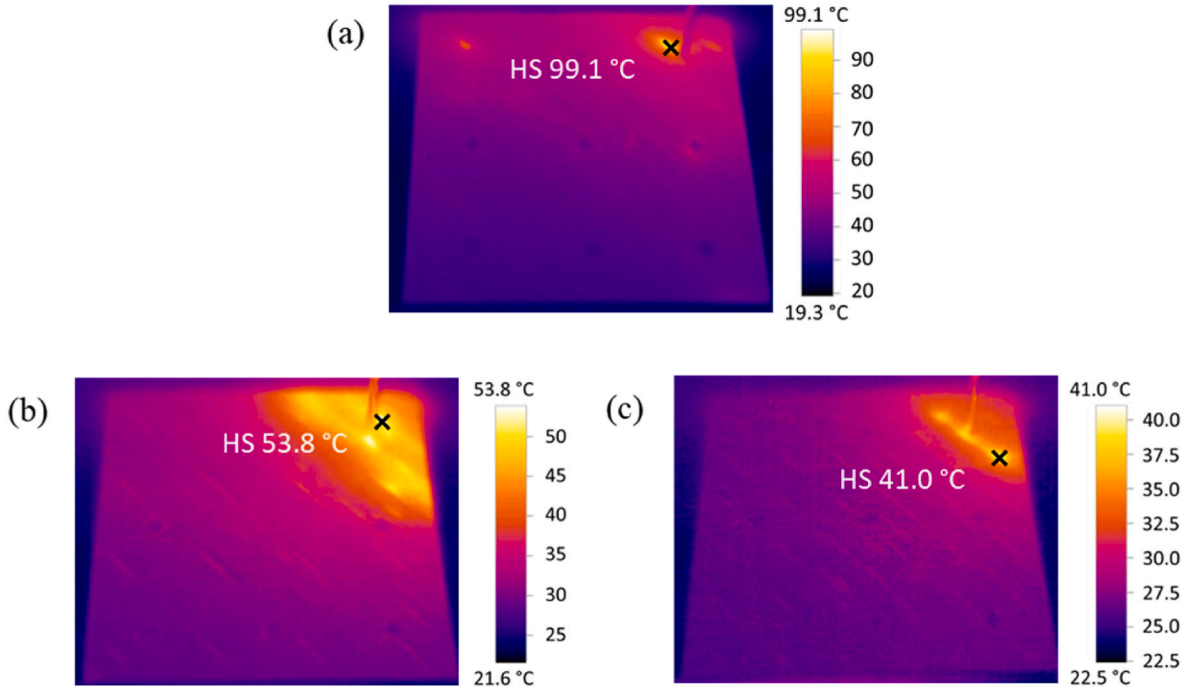

Fig. 14. In-plane thermal images: (a) UP-0.2A, (b) CAR-L-0.2A, (c) CAR-H-0.2A.

angle on the electrical conductivity and fault current response of Z-pinned composites.

CRediT authorship contribution statement

Mudan Chen: Conceptualization, Formal analysis, Investigation, Methodology, Validation, Writing – original draft. **Zhaobo Zhang:** Formal analysis, Investigation, Methodology, Writing – review & editing. **Bing Zhang:** Conceptualization, Formal analysis, Methodology, Supervision, Writing – review & editing. **Giuliano Allegri:** Conceptualization, Methodology, Supervision, Writing – review & editing. **Xibo Yuan:** Resources, Writing – review & editing. **Stephen R. Hallett:** Conceptualization, Methodology, Project administration, Supervision, Writing – review & editing.

Declaration of competing interest

The authors declare that they have no known competing financial interests or personal relationships that could have appeared to influence the work reported in this paper.

Data availability

Data will be made available on request.

Acknowledgements

This work was supported by the Engineering and Physical Sciences Research Council (EPSRC) through the Centre for Doctoral Training in Advanced Composites for Innovation and Science [grant number EP/L016028/1]. We are grateful for Mr. Juefei Yang and Mr. Renze Yu for supporting the tests.

Appendix A. Supplementary data

Supplementary data to this article can be found online at https://doi.org/10.1016/j.compscitech.2024.110466.

References

[1] A. Barzkar, M. Ghassemi, Electric power systems in more and all electric aircraft: a review, IEEE Access 8 (2020) 169314–169332, https://doi.org/10.1109/ACCESS.2020.3024168.
[2] C.E. Jones, P.J. Norman, G.M. Burt, C. Hill, G. Allegri, J. Yon, I. Hamerton, R. S. Trask, A route to sustainable aviation: a roadmap for the realization of aircraft components with electrical and structural multifunctionality, IEEE Trans. Transport.Electrific. 7 (2021) 3032–3049, https://doi.org/10.1109/TTE.2021.3078118.
[3] P. Preeti, C.E. Jones, P.J. Norman, G.M. Burt, Electrical Protection Solutions Enabling Integrated Electrical Power and Composite Structure Systems for Aircraft, 2022. https://ieeexplore.ieee.org/abstract/document/9841685.
[4] C.E. Jones, M. Sztykiel, R. Peña-Alzola, P.J. Norman, G.M. Burt, Grounding topologies for resilient, integrated composite electrical power systems for future aircraft applications, in: 2019 AIAA/IEEE Electric Aircraft Technologies Symposium (EATS), 2019, pp. 1–15, https://doi.org/10.2514/6.2019-4402.
[5] S. Das, T. Yokozeki, A brief review of modified conductive carbon/glass fibre reinforced composites for structural applications: lightning strike protection, electromagnetic shielding, and strain sensing, Composites Part C: Open Access 5 (2021) 100162, https://doi.org/10.1016/j.jcomc.2021.100162.
[6] C.E. Jones, P.J. Norman, M. Sztykiel, R. Pena Alzola, G.M. Burt, S.J. Galloway, L. F. Kawashita, S.R. Hallett, Electrical and thermal effects of fault currents in aircraft electrical power systems with composite aerostructures, IEEE Trans. Transp. Electrific. 4 (2018) 660–670, https://doi.org/10.1109/TTE.2018.2833838.
[7] A. Piche, D. Andissac, I. Revel, B. Lepetit, Dynamic electrical behaviour of a composite material during a short circuit, in: 10th International Symposium on Electromagnetic Compatibility, 2011, pp. 128–132. https://ieeexplore.ieee.org/document/6078540.
[8] A.P. Mouritz, Review of z-pinned laminates and sandwich composites, Compos. Appl. Sci. Manuf. 139 (2020) 106128, https://doi.org/10.1016/j.compositesa.2020.106128.
[9] F. Pegorin, K. Pingkarawat, A.P. Mouritz, Controlling the electrical conductivity of fibre-polymer composites using z-pins, Compos. Sci. Technol. 150 (2017) 167–173, https://doi.org/10.1016/j.compscitech.2017.07.018.
[10] K. Grigoriou, R.B. Ladani, A.P. Mouritz, Electrical properties of multifunctional Z-pinned sandwich composites, Compos. Sci. Technol. 170 (2019) 60–69, https://doi.org/10.1016/j.compscitech.2018.11.030.
[11] F. Pegorin, K. Pingkarawat, A.P. Mouritz, Numerical analysis of the heat transfer properties of z-pinned composites, Compos. Commun. 8 (2018) 14–18, https://doi.org/10.1016/j.coco.2018.03.002.
[12] M. Li, Z. Fang, S. Wang, Y. Gu, Y. Li, Z. Zhang, Thermal conductivity enhancement and heat transport mechanism of carbon fiber z-pin graphite composite structures, Compos. B Eng. 172 (2019) 603–611, https://doi.org/10.1016/j.compositesb.2019.05.092.
[13] M. Li, Z. Fang, S. Wang, Y. Gu, W. Zhang, Thermal conductivity enhancement and synergistic heat transfer of z-pin reinforced graphite sheet and carbon fiber hybrid composite, Int. J. Heat Mass Tran. 171 (2021) 121093, https://doi.org/10.1016/j.ijheatmasstransfer.2021.121093.
[14] M. Chen, B. Zhang, S. Friedemann, G. Allegri, S.R. Hallett, Effects of ferromagnetic & carbon-fibre Z-pins on the magnetic properties of composites, Compos. Sci. Technol. (2021) 108749, https://doi.org/10.1016/j.compscitech.2021.108749.
[15] B. Zhang, G. Allegri, S.R. Hallett, An experimental investigation into multi-functional Z-pinned composite laminates, Mater. Des. 108 (2016) 679–688, https://doi.org/10.1016/j.matdes.2016.07.035.
[16] B. Zhang, G. Allegri, M. Yasaee, S.R. Hallett, I.K. Partridge, On the delamination self-sensing function of Z-pinned composite laminates, Compos. Sci. Technol. 128 (2016) 138–146, https://doi.org/10.1016/j.compscitech.2016.03.019.
[17] F. Pegorin, K. Pingkarawat, A.P. Mouritz, Electrical-based delamination crack monitoring in composites using z-pins, Compos. Appl. Sci. Manuf. 104 (2018) 120–128, https://doi.org/10.1016/j.compositesa.2017.10.025.
[18] M. Kadlec, R. Růžek, P. Bělský, Concurrent use of Z-pins for crack arrest and structural health monitoring in adhesive-bonded composite lap joints, Compos. Sci. Technol. 188 (2020) 107967, https://doi.org/10.1016/j.compscitech.2019.107967.
[19] B. Zhang, S.R. Hallett, G. Allegri, Sensing delamination in composites reinforced by ferromagnetic Z-pins via electromagnetic induction, Compos. Sci. Technol. 217 (2022) 109113, https://doi.org/10.1016/j.compscitech.2021.109113.
[20] T.K. O'Brien, M.W. Czabaj, J.A. Hinkley, S. Tsampas, E.S. Greenhalgh, G. McCombe, I.P. Bond, R. Trask. Combining Through-Thickness Reinforcement and Self-Healing for Improved Damage Tolerance and Durability ofComposites, 2013. https://ntrs.nasa.gov/citations/20130013399.
[21] J. Konlan, P. Mensah, S. Ibekwe, K. Crosby, G. Li, Vitrimer based composite laminates with shape memory alloy Z-pins for repeated healing of impact induced delamination, Compos. B Eng. 200 (2020) 108324, https://doi.org/10.1016/j.compositesb.2020.108324.
[22] T.W. Loh, R.B. Ladani, A. Ravindran, R. Das, E. Kandare, A.P. Mouritz, Z-Pinned composites with combined delamination toughness and delamination Self-Repair properties, Composites Part A, Appl. Sci. Manufact. 149 (2021) 106566, https://doi.org/10.1016/j.compositesa.2021.106566.
[23] HexPly_M21_global_DataSheet.pdf, 2022. https://www.hexcel.com.
[24] R. Sfar Zbed, S. Le Corre, V. Sobotka, Process-induced strains measurements through a multi-axial characterization during the entire curing cycle of an interlayer toughened Carbon/Epoxy prepreg, Compos. Appl. Sci. Manuf. 153 (2022) 106689, https://doi.org/10.1016/j.compositesa.2021.106689.
[25] K. Bilge, M. Papila, 10 - interlayer toughening mechanisms of composite materials, in: Q. Qin, J. Ye (Eds.), Toughening Mechanisms in Composite Materials, Woodhead Publishing, 2015, pp. 263–294, https://doi.org/10.1016/B978-1-78242-279-2.00010-X.
[26] G. Korb, J. Koráb, G. Groboth, Thermal expansion behaviour of unidirectional carbon-fibre-reinforced copper-matrix composites, Compos. Appl. Sci. Manuf. 29 (1998) 1563–1567, https://doi.org/10.1016/S1359-835X(98)00066-9.
[27] C. Hagart-Alexander, Chapter 21 - temperature measurement, in: W. Boyes (Ed.), Instrumentation Reference Book, fourth ed., Butterworth-Heinemann, Boston, 2010, pp. 269–326, https://doi.org/10.1016/B978-0-7506-8308-1.00021-8.
[28] B. Zhang, G. Allegri, M. Yasaee, S.R. Hallett, Micro-mechanical finite element analysis of Z-pins under mixed-mode loading, Compos. Appl. Sci. Manuf. 78 (2015) 424–435, https://doi.org/10.1016/j.compositesa.2015.07.006.